Experimental Section

Materials

All the reagents were of analytical grade and were used as received without further purification. $Ce(NO_3)_3·6H_2O$ (≥99.0%), $Na_2MoO_4·2H_2O$ (≥99.0%), thiourea (≥99.0%), Na_2SO_4 (≥99.0%), $NaNO_3$ (≥99.0%), $C_7H_6O_3$ (≥99.5%), NaOH (≥96%), $KNaC_4H_{12}O_{10}·4H_2O$ (≥99.9%), NaClO (≥99.9 wt %), $NaNO_2$ (≥99.0%), NH_4Cl (≥99.5%), $C_{12}H_{14}N_2·2HCl$ (≥99.0%), $C_6H_8N_2O_2S$ (≥99.5%) were provided from Sigma-Aldrich Chemical Reagent Co., Ltd. and Sinopharm Chemical Reagent Co., Ltd.

Synthesis of Ce-MoS_{2-x} nanosheets

A piece of carbon cloth (CC, 2 cm × 4 cm) was ultrasonically treated in concentrated HCl for 2 h, followed by cleaning with ethanol and distilled water several times. Then, 4 mmol of thiourea and 1 mmol of $NaMo_4·2H_2O$ were dissolved in 40 mL of deionized water under stirring for 10 min, followed by addition of 0.1 mmol of $Ce(NO_3)_3·6H_2O$ under stirring for another 10 min. The mixed solution was then transferred into a Teflon-lined stainless-steel autoclave, followed by immersing the pretreated CC in the solution. The autoclave was sealed and maintained at 220 ℃ for 24 h. After cooling to room temperature, the obtained Ce-MoS_{2-x}/CC was washed with deionized water and ethanol several times, and dried at 60 ℃ overnight. For comparison, the pristine MoS_2/CC was prepared by the same procedure without addition of $Ce(NO_3)_3·6H_2O$.

Electrochemical experiments

Electrochemical measurements were tested on a CHI-660E electrochemical workstation in a three-electrode configuration including working electrode (Ce-MoS_2/CC), reference electrode (Hg/HgO), and counter electrode (platinum foil). All potentials were referenced to reversible hydrogen electrode (RHE) by following equation: $E_{(RHE)} = E_{(Hg/HgO)} + (0.098 + 0.0591 \times pH)$. The area of the working electrode immerse in electrolyte is 1 cm^2. The whole experiment was conducted under ambient conditions. The aqueous and gas product were detected by the colorimetric

methods and gas chromatography (GC), respectively. The detailed determination procedures are given in our previous publication[1].

Calculations of NH_3 yield and Faradaic efficiency

$$NH_3 \text{ yield} = (c \times V) / (17 \times t \times A) \quad (1)$$

$$FE = (8 \times F \times c \times V) / (17 \times Q) \times 100\% \quad (2)$$

where c (μg mL^{-1}) is the measured NH_3 concentration, V (mL) is the volume of electrolyte in the cathode chamber (30 mL), t (s) is the electrolysis time and A is the surface area of CC (1×1 cm^2), F (96500 C mol^{-1}) is the Faraday constant, Q (C) is the total quantity of applied electricity.

Characterizations

X-ray diffraction (XRD) pattern was recorded on a Rigaku D/max 2400 diffractometer. Scanning electron microscopy (SEM) was carried out on a JSM-6701 microscope. Transmission electron microscopy (TEM), high-resolution transmission electron microscopy (HRTEM), selected area electron diffraction (SAED) and high-angle annular dark field (HAADF) were performed on a Tecnai G^2 F20 microscope. X-ray photoelectron spectroscopy (XPS) analysis was performed on a PHI 5702 spectrometer. Electron paramagnetic resonance (EPR) measurements were performed on a Bruker ESP-300 spectrometer. UV-vis absorption spectra were measured on MAPADA ULM 1912006 UV-vis spectrophotometer.

Calculation details

DFT calculations were carried out using a Cambridge sequential total energy package (CASTEP).[2] The Perdew-Burke-Ernzerhof (PBE) generalized gradient approximation (GGA) functional was used for the exchange-correlation potential. The DFT-D correction method was considered for van der Waals forces. During the geometry optimization, the convergence tolerance was set to be 1.0×10^{-5} eV for energy and 0.02 eV $Å^{-1}$ for force. The Brillouin zone was sampled in a 1 × 1 × 1 mesh. The electron wave functions were expanded using plane waves with a cutoff energy of 520 eV. MoS_2 (001) was modeled by a 4 × 4 supercell, and a vacuum region of 15 Å was used to separate adjacent slabs.

The free energies (ΔG, 298 K) for each reaction were given after correction:

$$\Delta G=\Delta E+\Delta ZPE-T\Delta S \quad (3)$$

where ΔE is the adsorption energy, ΔZPE is the zero-point energy difference and $T\Delta S$ is the entropy difference between the gas phase and adsorbed state.

For MD simulations, the electrolyte system was modeled by a cubic cell with placing catalyst at the center of the cell and randomly filling 2000 H_2O, 36 NO_3^- and 36 Na^+. The force field type was chosen as universal. After geometry optimization, the MD simulations were performed in an NVT ensemble (298 K) with the total simulation time of 1 ns at a time step of 1 fs.

The radial distribution function (RDF) is calculated as

$$g(r) = \frac{dN}{4\pi\rho r^2 dr} \quad (4)$$

where dN is the amount of N_2 in the shell between the central particle r and $r+dr$, ρ is the number density of N_2.

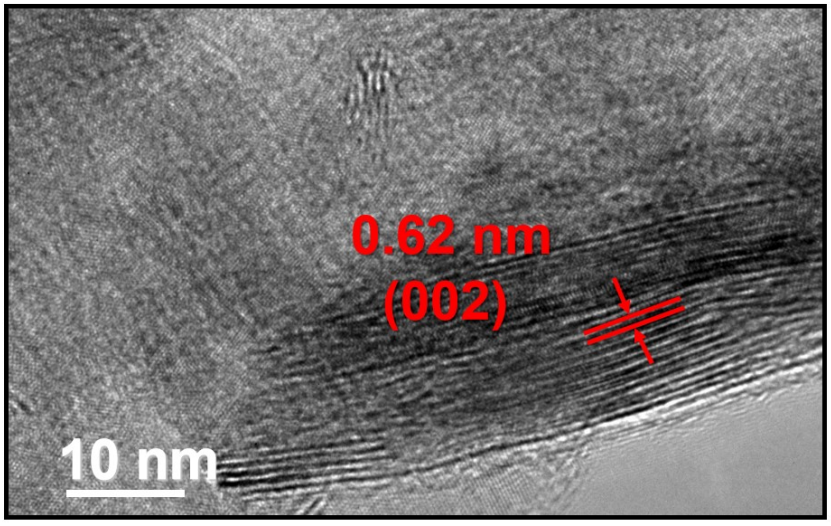

Fig. S1. HRTEM image of pristine MoS_2.

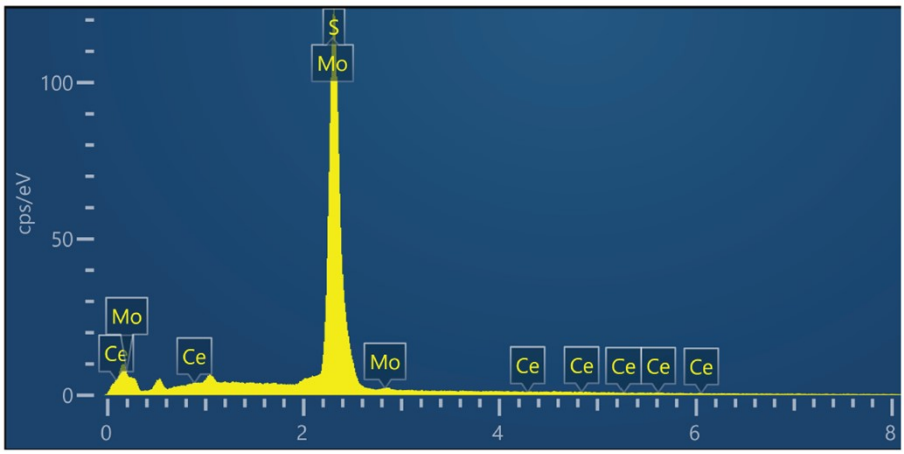

Fig. S2. EDS spectrum of Ce-MoS_{2-x}/CC.

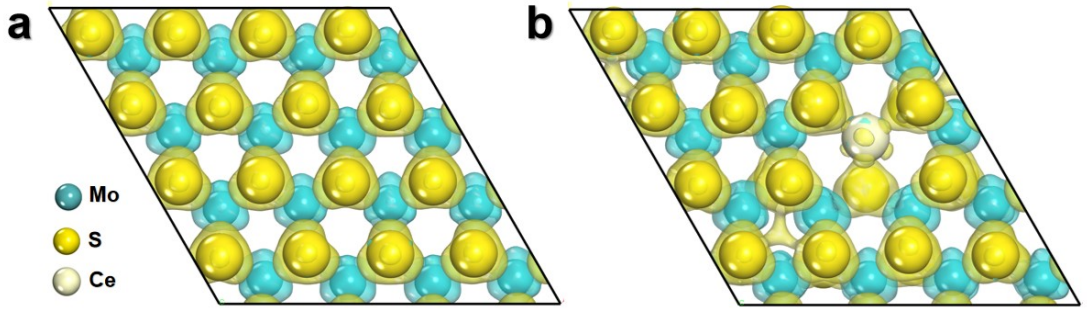

Fig. S3. Charge density distributions of (a) MoS_2 and (b) Ce-MoS_{2-x}. Yellow and cyan regions correspond to the electron accumulation and depletion, respectively.

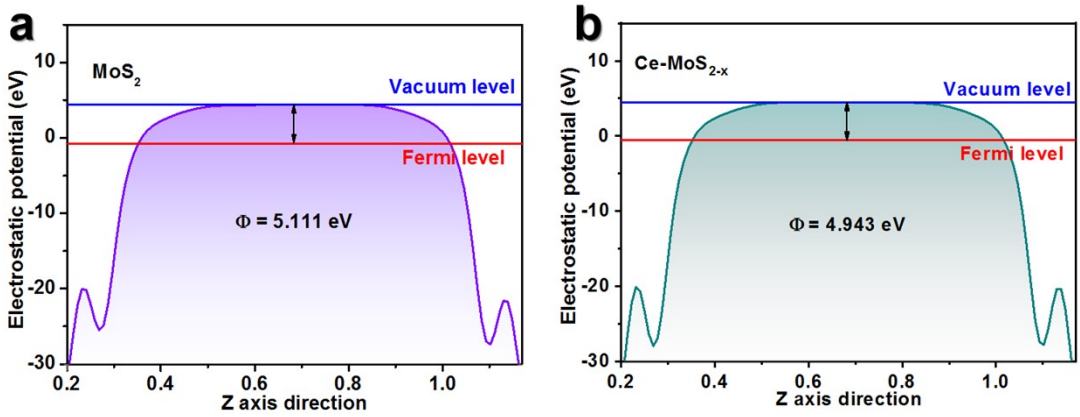

Fig. S4. Average potential profiles along c-axis direction for calculating the work functions of (a) MoS_2 and (b) Ce-MoS_{2-x}.

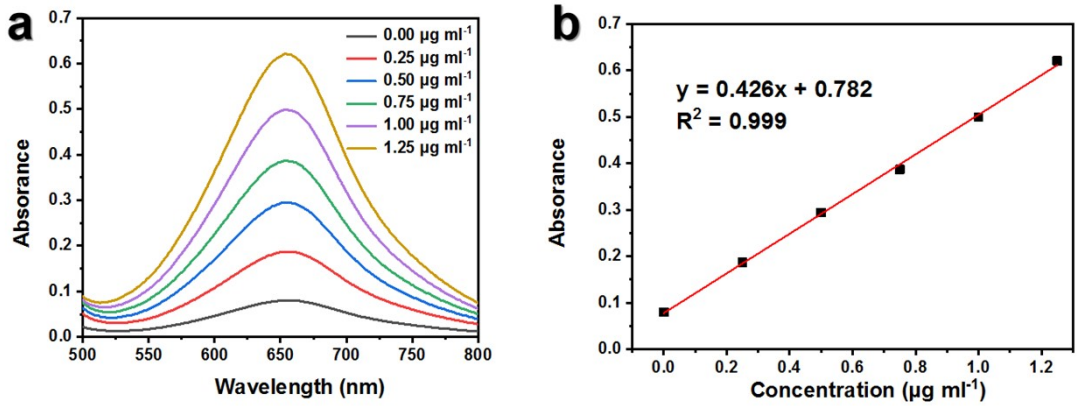

Fig. S5. (a) UV-vis absorption spectra of NH_4^+ assays after incubated for 2 h at ambient conditions. (b) Calibration curve used for calculation of NH_4^+ concentrations.

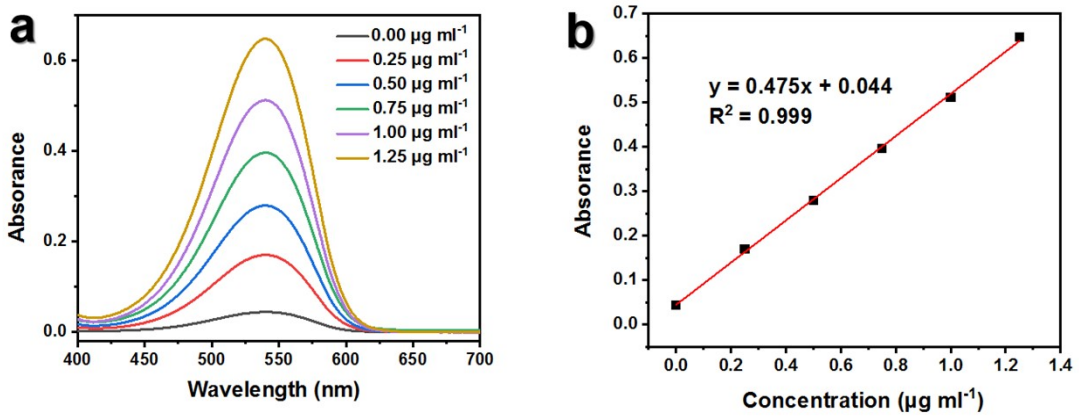

Fig. S6. (a) UV-vis absorption spectra of NO_2^- assays after incubated for 20 min at ambient conditions. (b) Calibration curve used for calculation of NO_2^- concentrations.

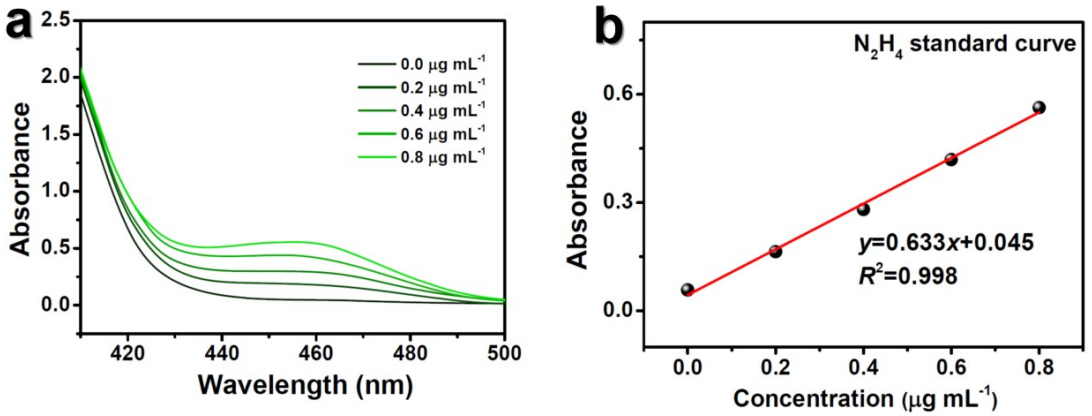

Fig. S7. (a) UV-vis absorption spectra of N_2H_4 assays after incubated for 20 min at ambient conditions. (b) Calibration curve used for calculation of N_2H_4 concentrations.

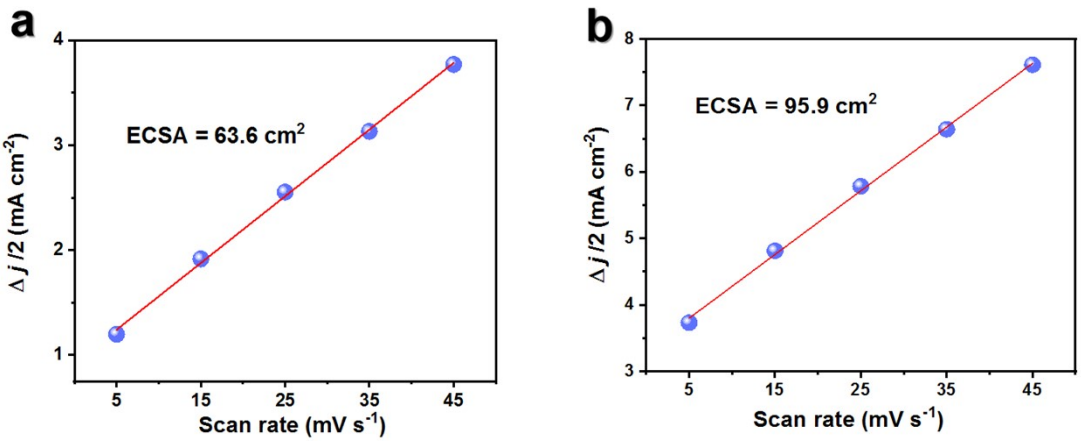

Fig. S8. Electrochemically active surface area measurements at different scanning rates of 5~45 mV s^{-1} for (a) MoS_2/CC and (b) Ce-MoS_{2-x}/CC.

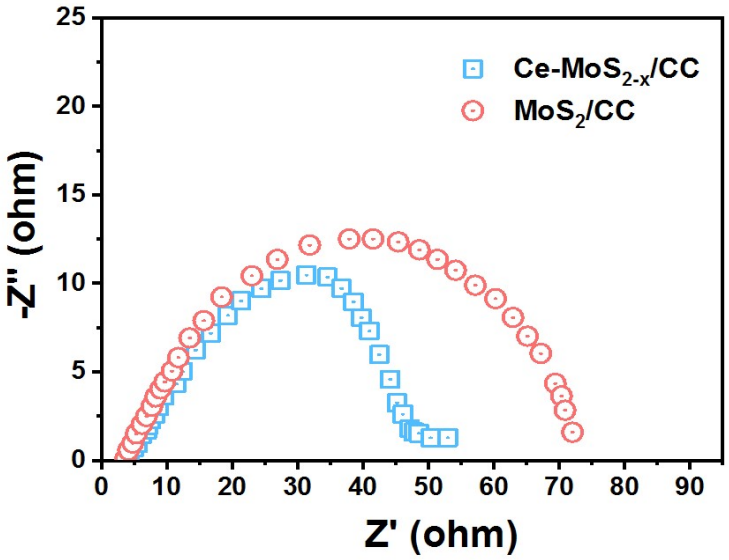

Fig. S9. Electrochemical impendence spectra of MoS_2/CC and Ce-MoS_{2-x}/CC.

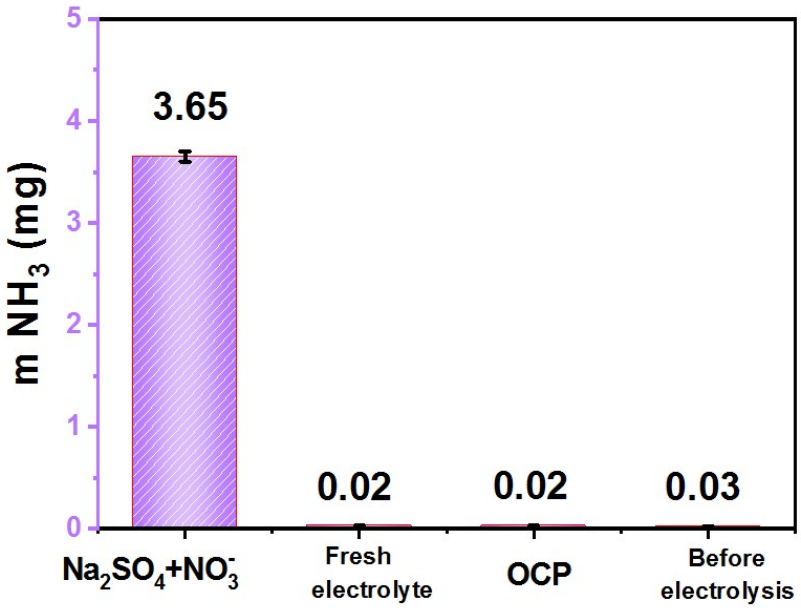

Fig. S10. Produced NH_3 of Ce-MoS_{2-x}/CC under different conditions at -0.7 V.

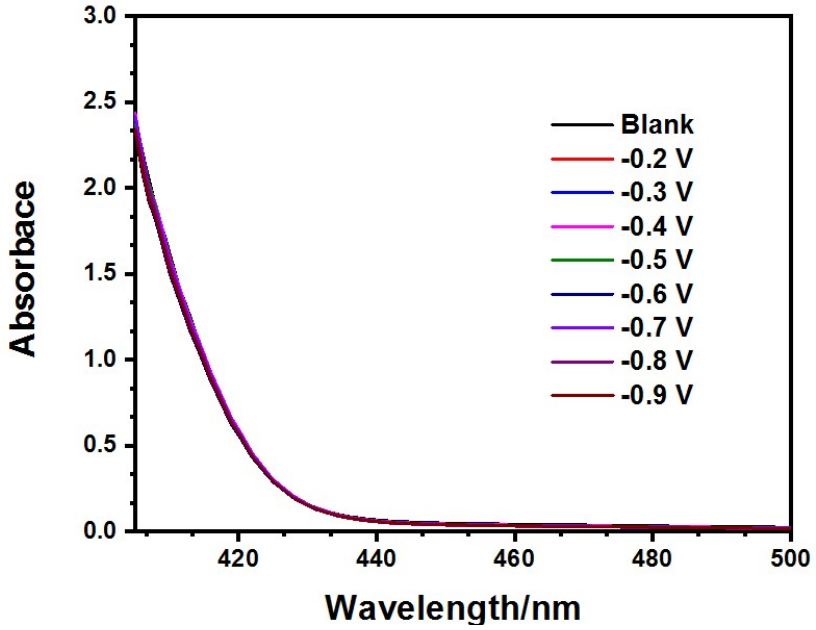

Fig. S11. UV-vis spectra of the electrolytes (stained with the chemical indicator based on the method of Watt and Chrisp) after 1h NO_3RR electrolysis on Ce-MoS_{2-x}/CC at various potentials.

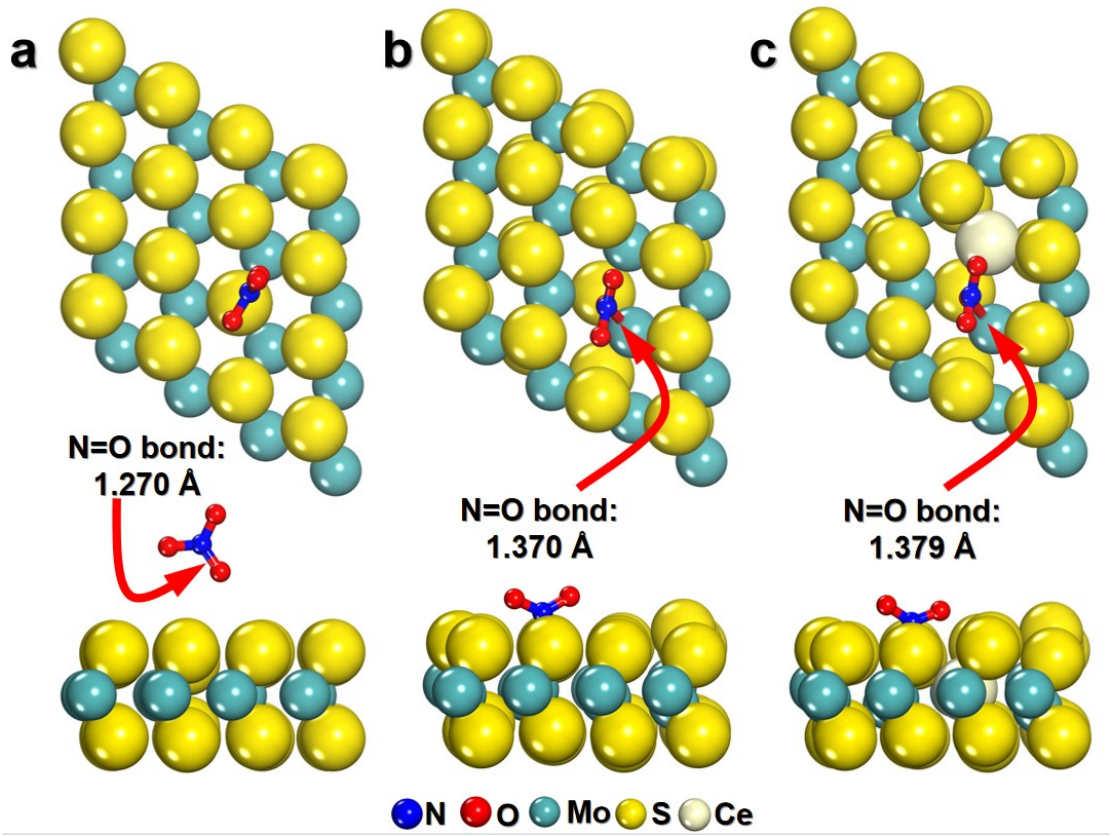

Fig. S12. Optimized structures of *NO_3 on pristine MoS_2, MoS_{2-x} and Ce-MoS_{2-x}.

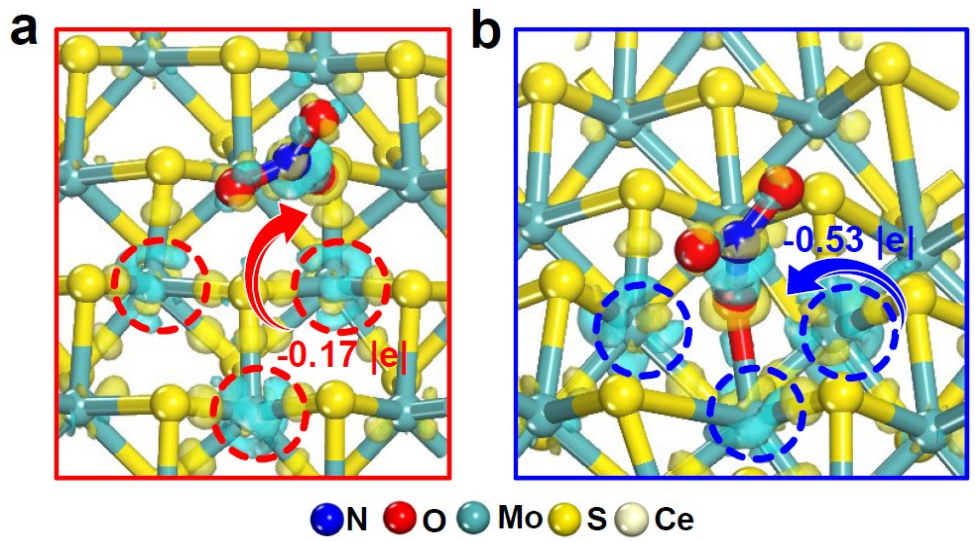

Fig. S13. Charge density difference plots of *NO_3 on (a) MoS_2 and (b) MoS_{2-x}.

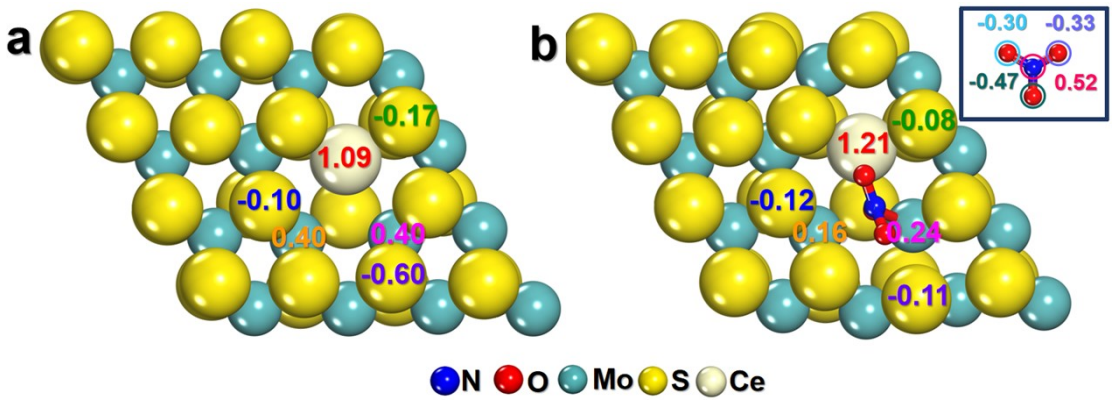

Fig. S14. Detailed charge analysis of (a) before and (b) after *NO_3 on Ce-MoS_{2-x}.

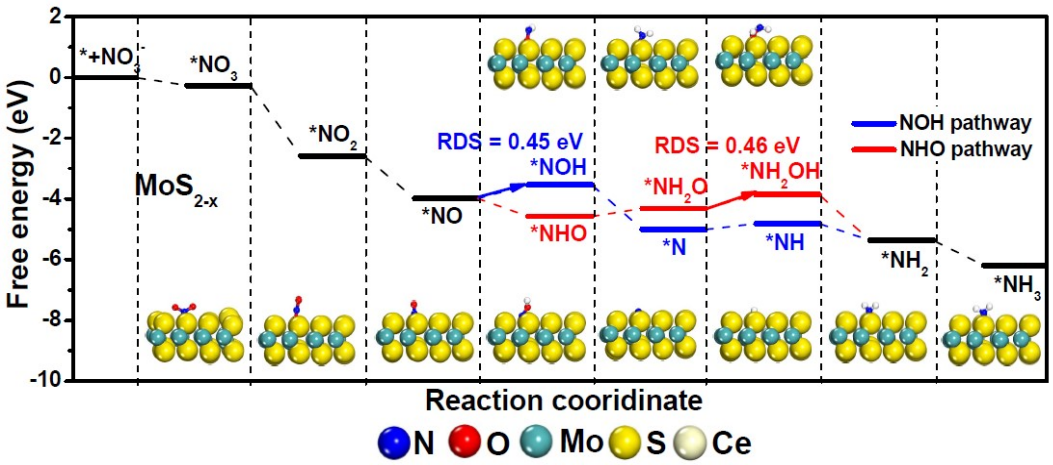

Fig. S15. Gibbs free energy diagrams of NO_3RR on MoS_{2-x}.

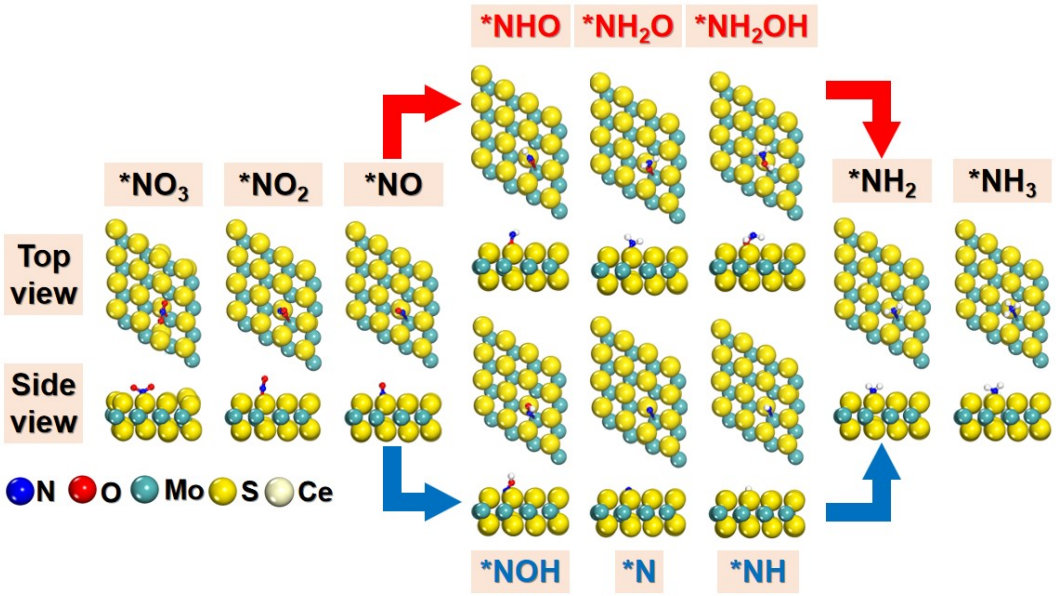

Fig. S16. Optimized structures of NO_3RR intermediates on MoS_{2-x}.

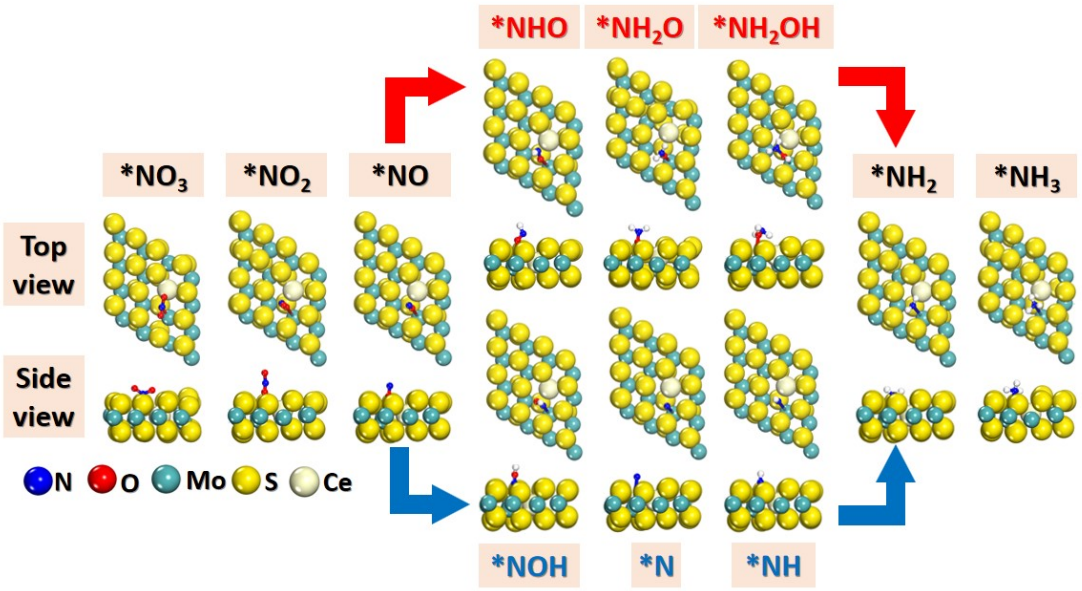

Fig. S17. Optimized structures of NO_3RR intermediates on Ce-MoS_{2-x}.

Table S1. Comparison of optimum NH_3 yield and Faradic efficiency (FE) for recently reported state-of-the-art NO_3RR electrocatalysts at ambient conditions.

Catalyst	Electrolyte	NH_3 yield rate	FE (%)	Potential (V vs RHE)	Ref.
Fe-doped Co_3O_4	0.1 M PBS (50 mM NO_3^-)	0.62 mg h^{-1} mg_{cat}^{-1}	95.5	-0.7	[3]
TiO_{2-x}	0.5 M Na_2SO_4 (50 ppm NO_3^-)	7.65 mg h^{-1} mg_{cat}^{-1}	85	-0.6	[4]
Fe_3C/NC	1 M KOH (5 mM KNO_3)	20.23 mg h^{-1} mg_{cat}^{-1}	96.7	-0.5	[5]
Fe-cyano NSs	1 M KOH (10 mM KNO_3)	42.1 mg h^{-1} mg_{cat}^{-1}	90.2	-0.5	[6]
CuO NWAs	0.5 M Na_2SO_4 (200 ppm NO_3^-)	4.16 mg $h^{-1}cm^{-2}$	95.8	-0.85	[7]
CoP/CC	1 M NaOH (2mM $NaNO_3$)	0.32 mg $h^{-1}cm^{-2}$	65	-0.4	[8]
Fe_3O_4/SS	0.1 M NaOH (0.1 M $NaNO_3$)	10.15 mg h^{-1} cm^{-2}	91.5	-0.5	[9]
Co_2AlO_4/CC	0.1 M PBS (0.1 M NO_3^-)	7.9 mg h^{-1} cm^{-2}	92.6	-0.7	[10]
$ZnCo_2O_4$ NSA/CC	0.1 M NaOH (0.1 M $NaNO_3$)	10.79 mg h^{-1} cm^{-2}	98.33	-0.6	[11]
Fe-MoS_2	0.1 M Na_2SO_4 (0.1 M $NaNO_3$)	0.51 mg $h^{-1}cm^{-2}$	98	-0.48	[12]
$NiCo_2O_4$/CC	0.1 M NaOH (0.1M $NaNO_3$)	16.54 mg h^{-1} cm^{-2}	99	-0.3	[13]
Ce-MoS_{2-x}/CC	**0.5 M Na_2SO_4 (0.1 M $NaNO_3$)**	**7.3 mg h^{-1} cm^{-2} 14.6 mg h^{-1} mg_{cat}^{-1}**	**96.6**	**-0.7**	**This work**

Supplementary references

[1]. K. Chen, Y. Luo, P. Shen, X. Liu, X. Li, X. Li and K. Chu, *Dalton Trans.*, 2022, **51**, 10343-10350.

[2]. S. J. Clark, M. D. Segall, C. J. Pickard, P. J. Hasnip, M. I. Probert, K. Refson and M. C. Payne, *Z Kristallogr Cryst Mater*, 2005, **220**, 567-570.

[3]. P. Wei, J. Liang, Q. Liu, L. Xie, X. Tong, Y. Ren, T. Li, Y. Luo, N. Li, B. Tang, A. M. Asiri, M. S. Hamdy, Q. Kong, Z. Wang and X. Sun, *J. Colloid Interface Sci.*, 2022, **615**, 636-642.

[4]. R. Jia, Y. Wang, C. Wang, Y. Ling, Y. Yu and B. Zhang, *ACS Catal.*, 2020, **10**, 3533-3540.

[5]. Y. Wang, L. Zhang, Y. Niu, D. Fang, J. Wang, Q. Su and C. Wang, *Green Chem.*, 2021, **23**, 7594-7608.

[6]. Z. Fang, Z. Jin, S. Tang, P. Li, P. Wu and G. Yu, *ACS nano*, 2021, **16**, 1072-1081.

[7]. Y. Wang, W. Zhou, R. Jia, Y. Yu and B. Zhang, *Angew. Chem., Int. Ed.*, 2020, **59**, 5350-5354.

[8]. H. Zhang, G. Wang, C. Wang, Y. Liu, Y. Yang, C. Wang, W. Jiang, L. Fu and J. Xu, *J. Electroanal. Chem.*, 2022, **910**, 116171.

[9]. X. Fan, L. Xie, J. Liang, Y. Ren, L. Zhang, L. Yue, T. Li, Y. Luo, N. Li, B. Tang, Y. Liu, S. Gao, A. A. Alshehri, Q. Liu, Q. Kong and X. Sun, *Nano Res.*, 2021, **15**, 3050–3055.

[10]. Z. Deng, J. Liang, Q. Liu, C. Ma, L. Xie, L. Yue, Y. Ren, T. Li, Y. Luo, N. Li, B. Tang, A. A. Alshehri, I. Shakir, P. O. Agboola, S. Yan, B. Zheng, J. Du, Q. Kong and X. Sun, *Chem. Eng. J*, 2022, **435**, 135104.

[11]. Z. Li, J. Liang, Q. Liu, L. Xie, L. Zhang, Y. Ren, L. Yue, N. Li, B. Tang, A. A. Alshehri, M. S. Hamdy, Y. Luo, Q. Kong and X. Sun, *Mater. Today Phys.*, 2022, **23**, 100619.

[12]. J. Li, Y. Zhang, C. Liu, L. Zheng, E. Petit, K. Qi, Y. Zhang, H. Wu, W. Wang and A. Tiberj, *Adv. Funct. Mater.*, 2022, **32**, 2108316.

[13]. Q. Liu, L. Xie, J. Liang, Y. Ren, Y. Wang, L. Zhang, L. Yue, T. Li, Y. Luo, N. Li, B. Tang, L. Yang, S. Gao, A. A. Alshehri, I. Shakir, P. O. Agboola, Q. Kong, Q. Wang, D. Ma and X. Sun, *Small*, 2022, **18**, 2106961.